Arabian Journal of Chemistry (2022) **15**, 103955

King Saud University

Arabian Journal of Chemistry

www.ksu.edu.sa
www.sciencedirect.com

ORIGINAL ARTICLE

Studies on the removal of phosphate in water through adsorption using a novel Zn-MOF and its derived materials

Yujie Zhang [a,b], Xinping Kang [a], Penghu Guo [a], Haijun Tan [b,*], Shu-Hua Zhang [a,b,*]

[a] *College of Chemistry, Guangdong University of Petrochemical Technology, Maoming, Guangdong 525000, PR China*
[b] *Guangxi Key Laboratory of Electrochemical and Magnetochemical Functional Materials, College of Chemistry and Bioengineering, Guilin University of Technology, Guilin 541004, PR China*

Received 17 March 2022; accepted 7 May 2022
Available online 13 May 2022

KEYWORDS

MOFs;
Carbonization;
Phosphate;
Adsorption performance

Abstract A novel zinc-based metal–organic framework, $\{[Zn_3(atz)_2(pda)_2]\cdot 2(H_2O)\}_n$ (**Zn-MOF**; Hatz is 5-aminote-1*H*-terazole; H_2pda is malonic acid), was prepared using the solvothermal method. Carbonization of the prepared **Zn-MOF** was conducted under elevated temperatures to investigate its phosphate adsorption performance. Through pre-adsorption experiments, the optimal carbonization temperature of 500 °C was determined, yielding **Zn-MOF-500**. Besides, multiple characterization methods were used to analyze the properties of **Zn-MOF** and **Zn-MOF-500** materials before and after the adsorption of phosphate ions. The results showed that the BET surface area of **Zn-MOF-500** was 18.57 m^2/g, which was 16.37 times larger than that of the BET surface area of **Zn-MOF**. At 25 °C, **Zn-MOF** and **Zn-MOF-500** exhibited an adsorption capacity of 123.44 and 226.07 mg/g, respectively. Based on the adsorption isotherms and the adsorption kinetics, the adsorption of PO_4^{3-} occurs via monolayer. X-ray diffractometry (XRD) and X-ray photoelectron spectroscopy (XPS) analysis showed that P was adsorbed on **Zn-MOF** and **Zn-MOF-500** as the zinc hydrogen phosphate and zinc phosphate ions, respectively.

1. Introduction

Phosphorus, a mineral nutrient, plays a vital role in plant growth. However, it can also cause serious eutrophication of water bodies when its concentration exceeds the permissible limit (Bacelo et al., 2020). Therefore, it is imperative to develop efficient and eco-friendly water dephosphorization methods. One of the most important strategies developed for dephosphorization is adsorption. However, traditional adsorption materials suffer from limitations such as low adsorption capac-

* Corresponding authors.
E-mail addresses: navytan@glut.edu.cn (H. Tan), Zhangshuhua@gdupt.edu.cn (S.-H. Zhang).
Peer review under responsibility of King Saud University.

ELSEVIER Production and hosting by Elsevier

https://doi.org/10.1016/j.arabjc.2022.103955
1878-5352

ity (Nuryadin et al., 2021) and difficult regeneration (Lin et al., 2015).

Metal-organic frameworks (MOFs), a new type of porous adsorption material (Wu et al., 2021a), have widely attracted the attention of researchers due to their compositional and structural variety, which has been realized by designing appropriate organic ligands and metal entities (Chen et al., 2019; Chen et al., 2020; Guan et al., 2018; Solanki and Borah, 2019; Wu et al., 2021b; Wang et al., 2021; Zhang et al., 2019; Zhang et al., 2020; Zhang et al., 2022). Since the initial report by the Kitagawa research group on the adsorption properties of MOFs in 1997, researchers began to explore the possibility of applying them more widely, especially in the field of wastewater treatment (Sumida et al., 2012; Zhang et al., 2021a). For example, Wang Yifei et al. prepared a composite of ZIF-8@MWCNT120 by growing ZIF-8 on hydroxylated multiwalled carbon nanotubes; the composite was found to have a maximum phosphate adsorption capacity of 203.0 mg/g (pH = 7) in water (Wang et al., 2020). Kun-Yi Andrew Lin et al. reported UiO-66-NH_2, which showed a maximum adsorption capacity of 92 mg/g at 20 °C (Lin et al., 2015). Arnab Ghosh and Gopal Das synthesized Sn(II)-MOF, which had a maximum adsorption capacity of 126.58 mg/g (Ghosh and Das, 2021). Although recent years have witnessed an increasing interest in the research on MOFs as adsorbents in wastewater treatment, their application is still restricted because of their low stability in aqueous media (Eltaweil et al., 2020). Because of the advantages of the traditional carbon-based materials (Karimi et al., 2020), MOF-derived carbon-containing composite materials obtained by high-temperature carbonization of MOFs are being applied widely in the field of wastewater treatment.

In this study, zinc acetate, malonic acid (H_2pda), and 5-amino-1*H*-tetrazole were used as the starting materials to synthesize a novel **Zn(II)-MOF**, which was post-synthetically treated under elevated temperatures to obtain MOF-derived carbon-containing materials. The properties of the synthesized materials were investigated using XRD, XPS, and SEM (Scanning electron microscope). Furthermore, studies on the removal of phosphate ions through adsorption from water and the corresponding reaction mechanism were conducted.

2. Experimental

*2.1. Synthesis of Zn-MOF and Zn-MOF-**n** (**n** = 300, 400, 500, 600, 700, and 800 °C)*

The information on the reagents and instruments in this study is listed in Supporting Information 1.1.

A mixture of Hatz (17 mg, 0.2 mmol), H_2pda (41.6 mg, 0.4 mmol), $Zn(OAc)_2{\cdot}2H_2O$ (0.0872 mg, 0.4 mmol), absolute ethanol (3.0 mL), acetonitrile (1.0 mL), and ultrapure water (4.0 mL) was placed in a 20 mL reactor and heated at 80–100 °C for 4–12 h. Colorless, long strip crystals of **Zn-MOF** were obtained by cooling the reactor to room temperature (yield: 0.0475 g, *ca.* 78.5% based on Hatz). *Anal. Calc.* for **Zn-MOF**: $C_8H_{12}N_{10}O_{10}Zn_3$ (M_r = 604.45), *calc.*: C, 15.90; H, 2.00; N, 23.18%; *found*: C, 15.82; H, 2.07; N, 23.26%. IR data for **Zn-MOF** (KBr, cm^{-1}, Fig. S1): 3396 s, 3242 s,1578 s, 1639 s, 1566 s, 1321 s, 1129 m, 969 m, 825 m, 763 s, 578 m, 463 w.

Due to the large amount of material required in the subsequent experiments, to facilitate the rapid synthesis of a large amount of **Zn-MOF** at one time in the subsequent experiments, a batch production experiment of **Zn-MOF** was carried out. In the experiment, raw materials whose dosage was increased by 10 times, and solution whose amount was increased by 7 times, were put into a 100 mL polytetrafluoroethylene reactor and placed in a 100 °C oven for 12 h. Colorless, long strip crystals of **Zn-MOF** were obtained by cooling the reactor to room temperature. Another method was that the raw materials and solutions which were in the same proportions were added into a 100 mL flask, and heated in a water bath at 80 °C for 12 h to produce **Zn-MOF**. After washing with absolute ethanol 3 times and drying, 3 reactors were chosen and calculated the average value to know that the average yield of **Zn-MOF** was 0.45 g. The purity of **Zn-MOF** was verified by XRD, the results are shown in Fig S3.

Zn-MOF-*n* was obtained by carbonizing the obtained **Zn-MOF** in a tube furnace at corresponding temperatures (300, 400, 500, 600, 700, and 800 °C) for 240 min and naturally cooling to room temperature.

2.2. Single-Crystal X-ray crystallography

Single-crystal X-ray diffraction data of **Zn-MOF** was collected on an Agilent G8910A CCD diffractometer with graphite monochromated Mo-Kα radiation (λ = 0.71073 Å) at 20 ± 1 °C by using the ω scan mode. Raw frame data were integrated with the SAINT program. The structure was solved by direct methods using SHELXT (Sheldrick, 2008, 2015) and refined by full-matrix least-squares on F^2 using SHELXL-2018 within the OLEX-2 GUI (Dolomanov et al., 2009). An empirical absorption correction was applied with spherical harmonics, implemented in SCALE3 ABSPACK scaling algorithm. All non-hydrogen atoms were refined anisotropically. All hydrogen atoms were positioned geometrically and refined as riding. Calculations and graphics were performed with SHELXTL (Sheldrick, 2008, 2015). The crystallographic details were provided in Table S1. Selected bond lengths and angles for **Zn-MOF** were listed in Table S2.

2.3. Adsorption experiment and characterization

The adsorption experiment, characterization methods, and calculation methods are detailed in Supporting Information 1.2.

3. Results and discussion

3.1. Description of the crystal structure

Single-crystal X-ray diffraction data of **Zn-MOF** revealed that the compound crystallizes in the monoclinic crystal system with the *I*2/*a* space group (Fig. 1 and Table S1). The asymmetric unit of the **Zn-MOF** was found to consist of a $[Zn_3(atz)_2(pda)_2]$ unit, with the two zinc atoms having different coordination environments. The Zn1 atom was coordinated with four O atoms from two different pda molecules [Zn1–O2 = 2.088(2) Å; Zn1–O3 = 2.045(2) Å; Zn1–O2A = 2.088(2) Å; Zn1–O3A = 2.045(2) Å] and two N atoms from two different atz molecules [Zn1–N3B = 2.158(2) Å; Zn1–N3C = 2.

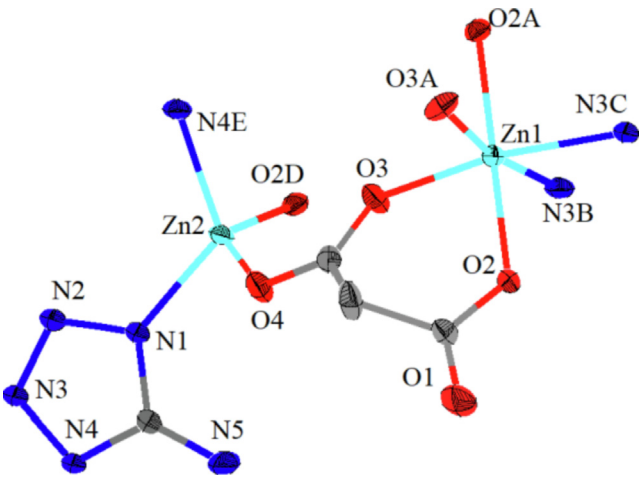

Fig. 1 Zn-MOF asymmetric unit structure diagram with 30% ellipsoid rate (symmetry: (A) $-x + 3/2, y, -z + 2$; (B) $x-1/2, y-1/2, z + 1/2$; (C) $-x + 2, y-1/2, -z + 3/2$; (D) $x + 1/2, -y + 1, z$; (E) ×, $-y + 3/2, z + 1/2$).

158(2) Å] (Fig. S2a and Table S2). The coordination configuration was found to be octahedron (label, OC-6; symmetry, O_h) using SHAPE 2.1 (Table S3). The Zn2 atom also displayed tetrahedron coordination (label, T-4; symmetry, T_d) by two O atoms from different pda molecules [Zn2–O4 = 1.948(2) Å; Zn2–O2D = 1.977(2) Å] and two N atoms from different atz molecules [Zn2–N1 = 2.006(2) Å; Zn2–N4E = 2.023(2) Å] (Fig. S2b and Table S2).

Two adjacent crystallographically independent Zn^{2+} atoms were connected through the carboxyl group on H_2pda, whose coordination mode was μ_2-η^2:η^1. **Zn-MOF** consists of the tortuous plane formed by Hatz, pda, and zinc atom, and then the longitudinal axis was connected to the two planes by pda to form a bridge (Fig. S2c). The stacking diagram had larger pores in the *a*-direction and diamond-like and elliptical pores in the *c*-direction (Fig. S2d and S2e). Based on PLATON calculations, each unit cell (1822.5 $Å^3$) of **Zn-MOF** was found to have a solvent-passable volume of 230.3 $Å^3$ and a porosity of 12.6% (excluding the solvent molecules). By comparing the actual measured XRD data and the results simulated by Mercury (Zhang et al., 2021b), the purity of the obtained sample was found to be sufficiently high (Fig. S3), and, therefore, could be used for subsequent carbonization experiments. IR data of **Zn-MOF** (KBr, cm^{-1}, Fig. S1): 3396 br, 3242 s, 1639 s, 1566 s, 1321 s, 1129 s, 969 m, 825 m, 763 s, 578 m, and 463 m.

3.2. Selecting the best carbonized material for phosphate adsorption

The phosphate adsorption capacity, q_e, of **Zn-MOF-*n*** (n = 300. 400, 500, 600, 700, and 800 °C) was found to increase with the increase in the feeding concentration, C_0 (Fig. 2a). The results indicated that the performance **of Zn-MOF-700** is slightly better than that of **Zn-MOF-500,** however, the preparation of zn-mof-700 needs more energy. So **Zn-MOF-500** was selected as the representative sample for use in subsequent experiments. In additional, the results also indicate that the material of **Zn-MOF-600** and **Zn-MOF-700** is just zinc oxide (PDF#89–0511, Fig. 2b) which is a known material. Therefore, we choose the carbonization temperature of 500 °C.

3.3. Selecting the optimized experimental conditions

As shown in Fig. 3c, the phosphate adsorption capacity and removal rate of **Zn-MOF-500** decreased with increasing pH. A pH value of 3 was considered to be the optimal pH. As shown in Table S4, when the temperature was 298.15 K and pH was 3, the phosphate ion existed mainly in the form of $H_2PO_4^-$ (87.985%) and H_3PO_4 (12.036%). As can be seen in Fig. 3a, the Zeta potential of **Zn-MOF-500** reduced with the decrease in pH. When the pH = 3, the Zeta potential was positive, which was beneficial for the electrostatic adsorption of phosphate (Liu et al., 2020).

When the pH was between 2 and 11 (Fig. 3b), the removal rate of **Zn-MOF** was very limited, approximately 30 mg/g. **Zn-MOF** showed maximum adsorption capacity and removal rate at pH = 7 when the phosphate ions existed mainly in the form of HPO_4^{2-} (39.687%) and $H_2PO_4^-$ (60.312%) (Table S4). The Zeta potential of **Zn-MOF** was negative at pH = 7 and positive at pH = 9 (Fig. 3a). The results revealed that the adsorption of phosphate on **Zn-MOF** was mainly by the functional groups (Tang et al., 2021).

As can be seen in Fig. 3d, the phosphate removal rate of **Zn-MOF** gradually increased with the increase in dosage, finally reaching equilibrium. The removal rate was found to increase with the increase in the **Zn-MOF** dosing. The reason for the observation may be attributed to the following: the number of adsorption sited gradually increase with the increase in the quantity of the additive, which further led to the gradual increase in the removal rate because the concentration of the solution was fixed. Therefore, when the dosing quantity reached a certain volume and because the concentration of phosphate in the solution remains constant, the removal rate started increasing, resulting in a gradual decrease in the adsorption capacity. When the dosage was 0.020 g, the phosphate removal rate of **Zn-MOF** reached 98.40%, and the remaining concentration of phosphate was 0.330 mg/L.

Zn-MOF-500 had far more active sites than the original **Zn-MOF**, which resulted in a 99.47% removal rate of phosphate from a solution containing 20 mg/L of the ion, even when the dosage of the adsorbent was only 0.005 g (Fig. 3e). The phosphate remaining concentration of **Zn-MOF-500** was only 0.102 mg/L. For the convenience of subsequent experiments and comparing the performance of the two materials, the dosage of the two materials was maintained at 0.020 g.

3.4. Adsorption isotherms

Isothermal adsorption research is used to study the adsorption mechanism and is one of the important methods to obtain adsorption capacity. The adsorption isotherms of **Zn-MOF** and **Zn-MOF-500** under different temperatures were shown in Fig. 4, and the data on fitting were shown in Table 1 (Lian et al., 2021; Zhang et al., 2021c). In this study, all data of **Zn-MOF-500** fitted the Langmuir model better than the Freundlich model based on the R^2 values (Table 1), which indicated that the adsorption on **Zn-MOF-500** was mainly monolayer adsorption. All of the Langmuir model and Freundlich

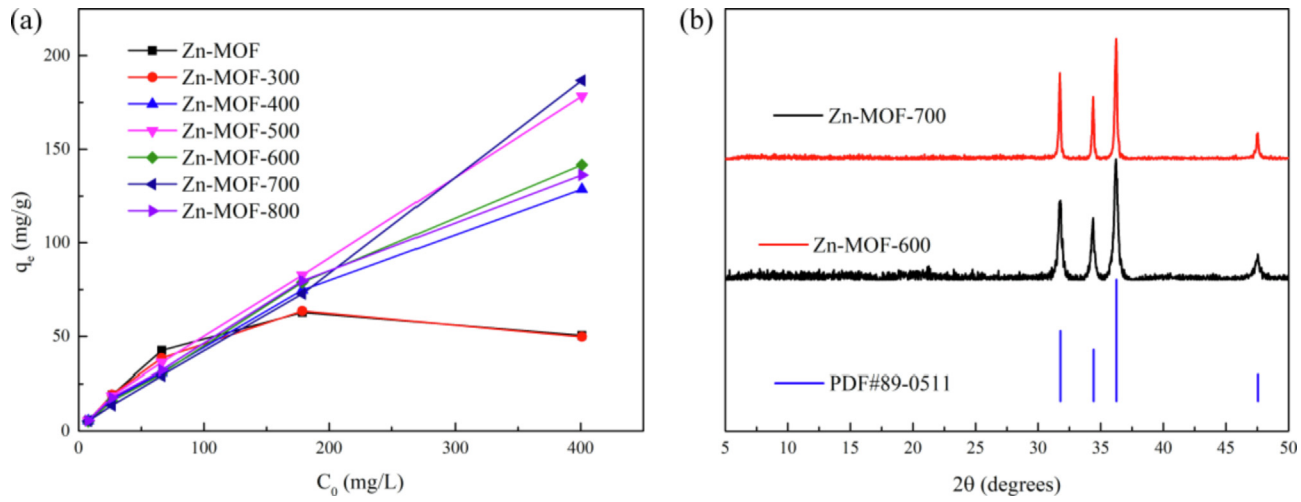

Fig. 2 (a)Phosphate adsorption performance of **Zn-MOF** and **Zn-MOF-n** at different feeding concentrations C_0; (b)The PXRD patterns of **Zn-MOF-600**, **Zn-MOF-700** and PDF card.

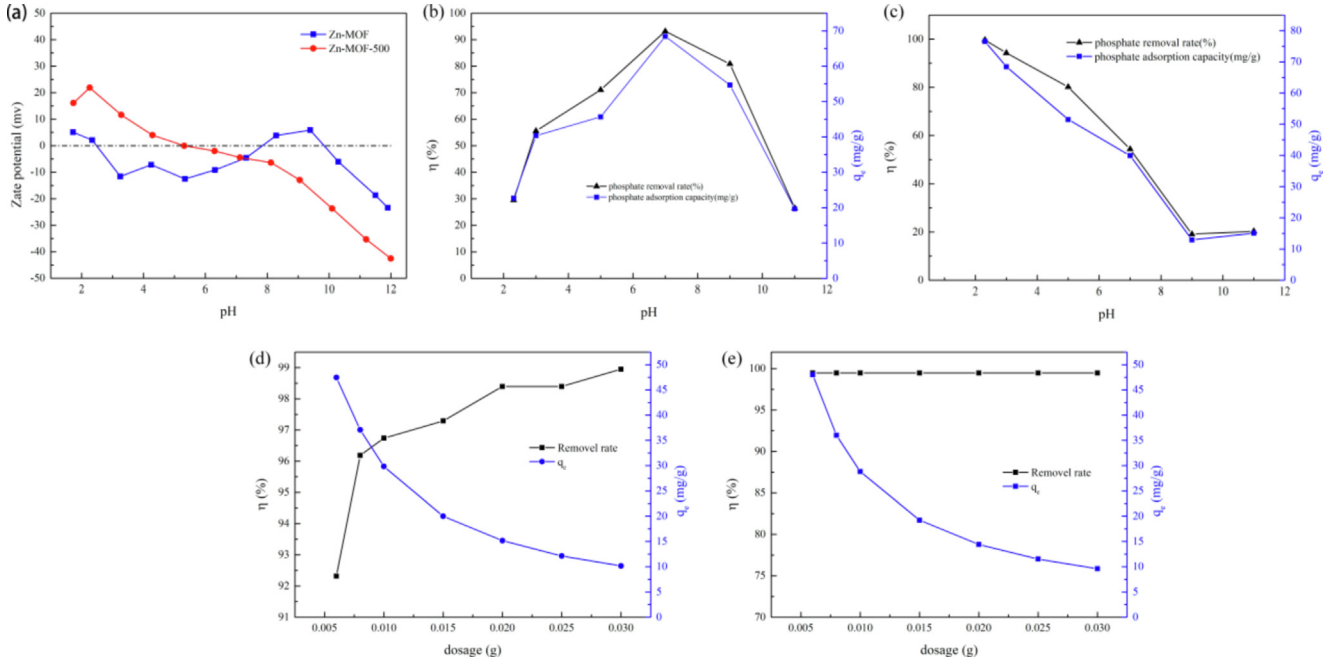

Fig. 3 (a) Zeta potential diagram of **Zn-MOF** and **Zn-MOF-500**; (b, c) Diagram of phosphate absorption rate and equilibrium adsorption capacity of **Zn-MOF** and **Zn-MOF-500** as a function of pH; (d, e) The absorption rate and equilibrium adsorption capacity of **Zn-MOF** and **Zn-MOF-500**.

model were fitted well by comparing the R^2 values of **Zn-MOF**; the data fitted the Langmuir model better than the Freundlich model at 298.15 and 308.15 K (Table 1) and fitted the Freundlich model better than the Langmuir model at 288.15 K. Therefore, it could be ascertained that the adsorption that occurred at the surface of the **Zn-MOF** was monolayer adsorption at 298.15 and 308.15 K and the adsorption that occurred in the pores of **Zn-MOF** was multilayer adsorption at 288.15 K. Both **Zn-MOF** and **Zn-MOF-500** were found to exhibit good performance when the adsorbed phosphate material was the same (Tables 2 and 3). **Zn-MOF-500** is second only to CM-300(R) in Table 3. However, since hydrazine hydrate, which is harmful to the environment, was used in the preparation of CM-300(R), **Zn-MOF-500** was found to be more suitable for practical use. Furthermore, the *n* values of **Zn-MOF** and **Zn-MOF-500** in the Freundlich model were more than 1, which showed that adsorption occurred easily (Table 1) (Rukayat et al., 2021).

3.5. Adsorption kinetics

The pseudo-first-order and pseudo-second-order kinetics are used to fit the nonlinear dynamics of **Zn-MOF** and **Zn-MOF-500** at 288.15 K, 298.15 K, and 308.15 K (Fig. 5). All

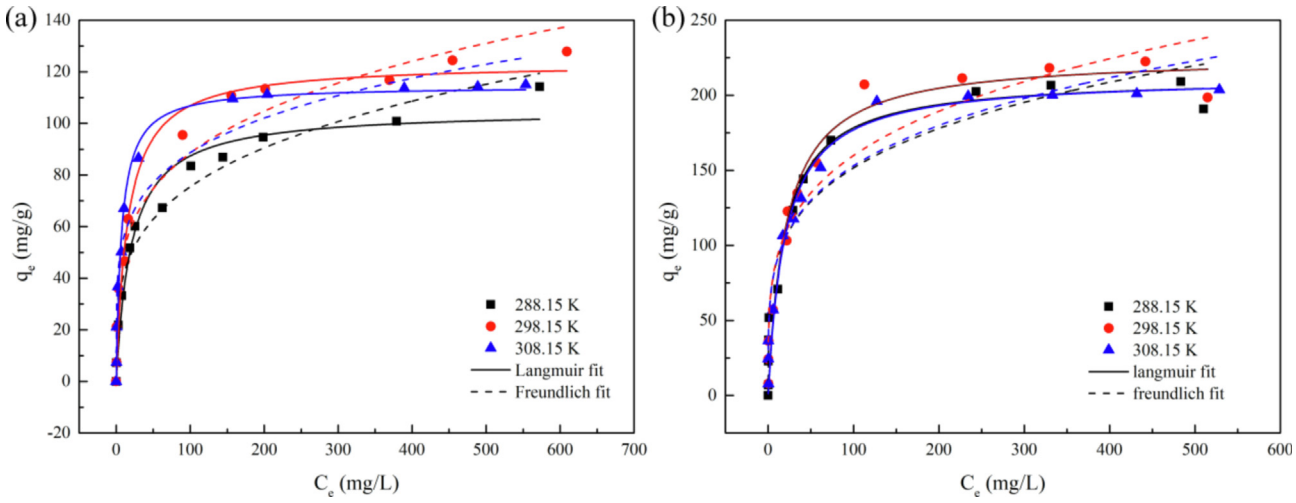

Fig. 4 (a, b) Langmuir and Freundlich nonlinear fitting of **Zn-MOF** and **Zn-MOF-500** at 288.15 K, 298.15 K, 308.15 K.

Table 1 Fitting results of Langmuir and Freundlich model for phosphate adsorption on **Zn-MOF** and **Zn-MOF-500**.

Complexes	T/K	Langmuir			Freundlich		
		q_{max}/ (mg/g)	B/(L/mg)	R^2	K_F	n	R^2
Zn-MOF	288.15	105.20	0.049	0.967	22.47	3.80	0.970
	298.15	123.44	0.065	0.967	28.72	4.09	0.966
	308.15	114.53	0.138	0.983	34.74	4.92	0.929
Zn-MOF-500	288.15	211.90	0.052	0.950	52.45	4.34	0.944
	298.15	226.07	0.048	0.965	51.92	4.09	0.914
	308.15	212.23	0.050	0.962	52.10	4.27	0.935

Table 2 Comparison of the adsorptive capacity of MOFs adsorbents for phosphate from water.

Adsorbents	Reaction conditions	q_{max}/(mg/g)	Ref.
Al-PMA	c_0 = 10–100 mg/L, [Ads.] = 0.2 g/L, pH = 7.0, T = 298.15 K	43.38	(Li et al., 2021)
Al-BPDC	c_0 = 10–100 mg/L, [Ads.] = 0.2 g/L, pH = 7.0, T = 298.15 K	55.46	(Li et al., 2021)
Al-BHTA	c_0 = 10–100 mg/L, [Ads.] = 0.2 g/L, pH = 7.0, T = 298.15 K	74.02	(Li et al., 2021)
UIO-66	c_0 = 1010 mg/L, [Ads.] = 1.5–18 g/L, pH = 4.0, T = 298.15 K	74.50	(Guan et al., 2020)
Al-BDC-NH_2	c_0 = 10–100 mg/L, [Ads.] = 0.2 g/L, pH = 7.0, T = 298.15 K	92.34	(Li et al., 2021)
Al-BDC	c_0 = 10–100 mg/L, [Ads.] = 0.2 g/L, pH = 7.0, T = 298.15 K	100.00	(Li et al., 2021)
Fe-MIL-88B	c_0 = 50–150 mg/L, [Ads.] = 1 g/L, T = 298.15 K	103.09	(Pandi and Choi 2021)
CM[a]	c_0 = 25–1000 mg/L, [Ads.] = 1 g/L, pH = 6.0, T = 298.15 K	105.00	(He et al., 2020a)
MIL-101(Fe)	c_0 = 0.6–60 mg/L, [Ads.] = 0.06 g/L, T = 293 K	107.70	(Xie et al. 2017)
UIO-66-NO_3	c_0 = 1010 mg/L, [Ads.] = 1.5–18 g/L, pH = 4.0, T = 298.15 K	117.70	(Guan et al., 2020)
Zn-MOF	c_0 = 10–600 mg/L, [Ads.] = 1.33 g/L, pH = 7.0, T = 298.15 K	123.44	This work
NH_2-MIL-101(Fe)	c_0 = 0.6–60 mg/L, [Ads.] = 0.06 g/L, T = 293 K	124.38	(Xie et al. 2017)
UIO-66-Br	c_0 = 1010 mg/L, [Ads.] = 1.5–18 g/L, pH = 4.0, T = 298.15 K	132.50	(Guan et al., 2020)
UIO-66-NH_2	c_0 = 1010 mg/L, [Ads.] = 1.5–18 g/L, pH = 4.0, T = 298.15 K	153.90	(Guan et al., 2020)

[a] $\{[Ce(BTC)(H_2O)]\cdot DMF\}_n$.

experimental data fitted the pseudo-second-order kinetics better than the pseudo-first-order kinetics, based on the R^2 values (Table 4). The results indicated that the adsorption capacity was proportional to the square of the driving force and that chemical adsorption took place on both materials (Lian et al., 2021). At 308.15 K, the reaction rate constant k_2 of **Zn-MOF-500** was higher than that at 288.15 K, but its equilibrium adsorption capacity was less than that at 288.15 K.

To determine whether the intraparticle diffusion was the rate-limiting step in the adsorption process, the data of **Zn-MOF** and **Zn-MOF-500** were fitted to the intraparticle diffusion model (Table 5).

As shown in Fig. S4 and Table 5, the adsorption of phosphate on **Zn-MOF** and **Zn-MOF-500** was divided into two stages where each fitting point had a linear relationship in multiple segments. In addition, since the fitting curves of the three adsorption stages did not pass through the origin, it indicated

Table 3 Comparison of the adsorptive capacity of carbonization MOFs adsorbents for phosphate from water.

Adsorbents	Reaction conditions	q_{max}/(mg/g)	Ref.
Ce-MOF-500(U)[a]	c_0 = 50–500 mg/L, [Ads.] = 1 g/L, pH = 6.0, T = 298.15 K	82.30	(He et al., 2020b)
La-MOF-500	c_0 = 40–100 mg/L, [Ads.] = 0.2 g/L, T = 298.15 K	173.80	(Zhang et al., 2017)
Ce-MOF-500(S)[b]	c_0 = 50–500 mg/L, [Ads.] = 1 g/L, pH = 6.0, T = 298.15 K	189.40	(He et al., 2020b)
CM-150(R)[c]	c_0 = 25–1000 mg/L, [Ads.] = 1 g/L, pH = 6.0, T = 298.15 K	204.00	(He et al., 2020a)
Zn-MOF-500	c_0 = 10–500 mg/L, [Ads.] = 1.33 g/L, pH = 3.0, T = 298.15 K	226.07	This work
CM-300(R)[c]	c_0 = 25–1000 mg/L, [Ads.] = 1 g/L, pH = 6.0, T = 298.15 K	273.00	(He et al., 2020a)

[a] MOF is kept constant at 500 °C for 3 h in air environment.
[b] MOF is kept constant at 500 °C for 3 h in N_2 environment.
[c] Reduction of carbon-based MOF materials with hydrazine hydrate.

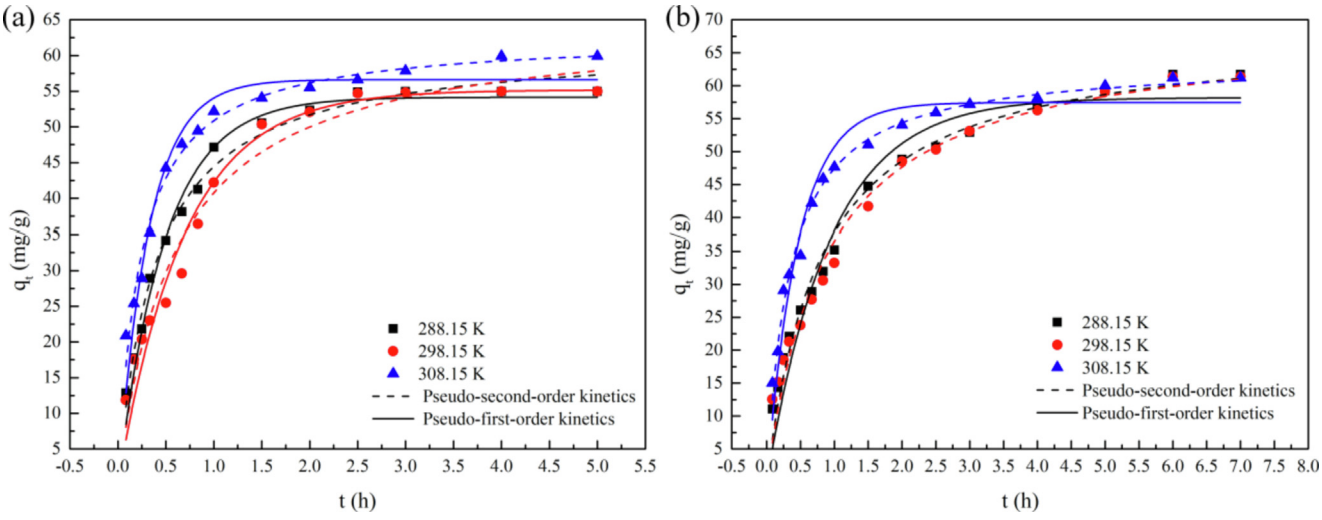

Fig. 5 Pseudo-first-order kinetic (a) and pseudo-second-order kinetic (b) nonlinear dynamics fitting of **Zn-MOF** and **Zn-MOF-500** at 288.15 K, 298.15 K and 308.15 K.

Table 4 Fitting results of Pseudo-first-order kinetic and Pseudo-second-order kinetic for phosphate adsorption on **Zn-MOF** and **Zn-MOF-500**.

Complex	T/K	$q_{e,exp}$	Pseudo-first-order kinetics			Pseudo-second-order kinetics		
			q_{eq}/(mg/g)	k_1/h^{-1}	R^2	q_{eq}	k_2/(g/[(mg·h)])	R^2
Zn-MOF	288.15	54.98	54.16	2.04	0.982	61.73	0.042	0.989
	298.15	54.98	55.25	1.45	0.962	64.78	0.026	0.966
	308.15	59.92	56.74	3.07	0.942	62.85	0.068	0.980
Zn-MOF-500	288.15	61.71	58.18	1.06	0.957	68.10	0.018	0.985
	298.15	61.37	58.37	0.973	0.947	68.60	0.010	0.975
	308.15	61.20	57.45	2.14	0.951	63.72	0.046	0.991

that the intraparticle diffusion rate was not the only parameter that controlled the adsorption of phosphate on **Zn-MOF** and **Zn-MOF-500** (Gao et al., 2021).

3.6. Regeneration of adsorbents and anti-interference

The regeneration efficiency of **Zn-MOF** and **Zn-MOF-500** when 0.1 mol/L NaCl solution was employed is depicted in Fig. S5 (Wang et al., 2020). When **Zn-MOF-500** was used as the adsorbent, the removal rate remained consistently above 80% even after 6 cycles; however, the removal rate dropped sharply after the first cycle itself when **Zn-MOF** was used as the adsorbent. When compared with that of **Zn-MOF-500**, the cycling performance of **Zn-MOF** was not appreciable. It was observed that carbonization improved the cycling performance of **Zn-MOF** because its removal rate dropped to less than 50% only after the second cycle.

To study the effect of competitive ions in the adsorption of phosphate, coexisting anions were focused, such as NO_3^-, Cl^-, SO_4^{2-}, and CO_3^{2-} in a 10 mg/L phosphate solution (Fig. 6). No obvious effect was observed in the case of **Zn-MOF-500** in a 0.1 mol/L solution of coexisting anions and **Zn-MOF**

Table 5 **Zn-MOF** and **Zn-MOF-500** intra-particle diffusion model fitting data table.

Complexes	T/K	The first stage			The second stage		
		K_p	C	R^2	K_p	C	R^2
Zn-MOF	288.15	47.80	−0.88	0.987	34.29	12.97	0.988
	298.15	40.60	−0.491	0.976	9.51	38.84	0.890
	308.15	47.12	7.29	0.968	7.04	45.42	0.986
Zn-MOF-500	288.15	35.09	0.824	0.994	13.47	29.24	0.969
	298.15	31.84	2.32	0.994	12.65	30.72	0.994
	308.15	46.69	2.76	0.971	8.85	40.57	0.929

was observed to perform better with a higher removal rate than the blank in a solution containing NO_3^- or Cl^-. Thus, it was concluded that **Zn-MOF-500** performed better in terms of adsorption capacity and anti-interference than **Zn-MOF.**

3.7. BET (Brunauer-Emmet-Teller)

The BET-specific surface area of **Zn-MOF** was 1.11 m^2/g and that of **Zn-MOF-500** was 18.57 m^2/g (Table 6). The BET-specific surface area of **Zn-MOF-500** was 16.73 times that of **Zn-MOF**.

The pore properties of **Zn-MOF** and **Zn-MOF-500** were obtained using the N_2 desorption test (Fig. S6). It was observed that **Zn-MOF** had no hysteresis loop and that the material was mainly concentrated in the micropores; however, the isotherm of **Zn-MOF-500** had an obvious hysteresis loop, it had no obvious saturated adsorption platform, indicating that the pore structure of **Zn-MOF-500** was highly irregular.

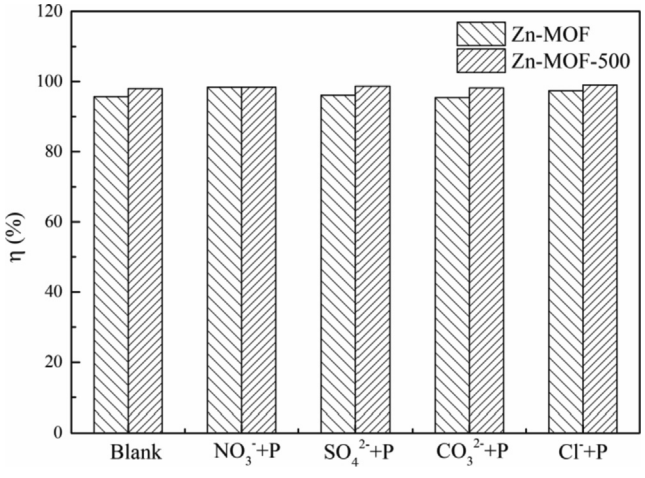

Fig. 6 Effect of co-existed anions on **Zn-MOF** and **Zn-MOF-500.**

3.8. Thermogravimetric

The thermogravimetric data of **Zn-MOF** and **Zn-MOF-500** are shown in Fig. S7. From Fig. S7a, the structure of **Zn-MOF** began to collapse at 322.3 °C and ended when heated to 368.8 °C, and then the remaining mass remains relatively stable until 700 °C, and the final production was zinc oxide. From Fig. S7b, **Zn-MOF-500** begins to lose weight at 620.6 °C. It observed that **Zn-MOF** and **Zn-MOF-500** had different weight loss trends, which indicated that the structure of **Zn-MOF** was destroyed after modification and that **Zn-MOF-500** exhibits strong thermal stability.

3.9. XRD and FT-IR (Fourier transform Infrared) spectra

The XRD data and FT-IR **spectra** of **Zn-MOF**, **Zn-MOF-500**, **Zn-MOF-500-P (Zn-MOF-500-P** is **Zn-MOF-500** after adsorption of phosphate**)**, and **Zn-MOF-P** (**Zn-MOF-P** is **Zn-MOF** after adsorption of phosphate) were shown in Fig. 7. Comparing the XRD peak position and peak value of **Zn-MOF and Zn-MOF-P (**Fig. 7a**)**, we found that the XRD peak position and peak value of **Zn-MOF-P** were significantly different from the **Zn-MOF**, indicating that the structures of the two materials are different. This result implies that **Zn-MOF** is unstable in aqueous solution. Comparing the XRD peak position and peak value of **Zn-MOF-500 and Zn-MOF-500-P (**Fig. 7b**)**, we found that the XRD peaks positions and peak value of the two materials were basically unchanged. This result implies that **Zn-MOF-500** is stable in aqueous solution. By comparing the FT-IR spectra of **Zn-MOF** and **Zn-MOF-500** with those of **Zn-MOF-P** and **Zn-MOF-500-P**, it was found that **Zn-MOF-P** and **Zn-MOF-500-P** showed strong peaks at 1058 and 1056 cm^{-1} (Fig. 7c,d), respectively, which proved that C—O (Acharya et al., 2020) underwent a stretching motion during the adsorption process and participated in the process.

Table 6 BET data of **Zn-MOF** and **Zn-MOF-500.**

Complexes	SSA(Langmuir) /g·m^{-2}	SSA(BET) /g·m^{-2}	Pore Volume(BJH) /g·cm^{-2}	Pore size /nm
Zn-MOF	2.28	1.11	0.0031	12.12
Zn-MOF-500	88.41	18.57	0.0677	15.52

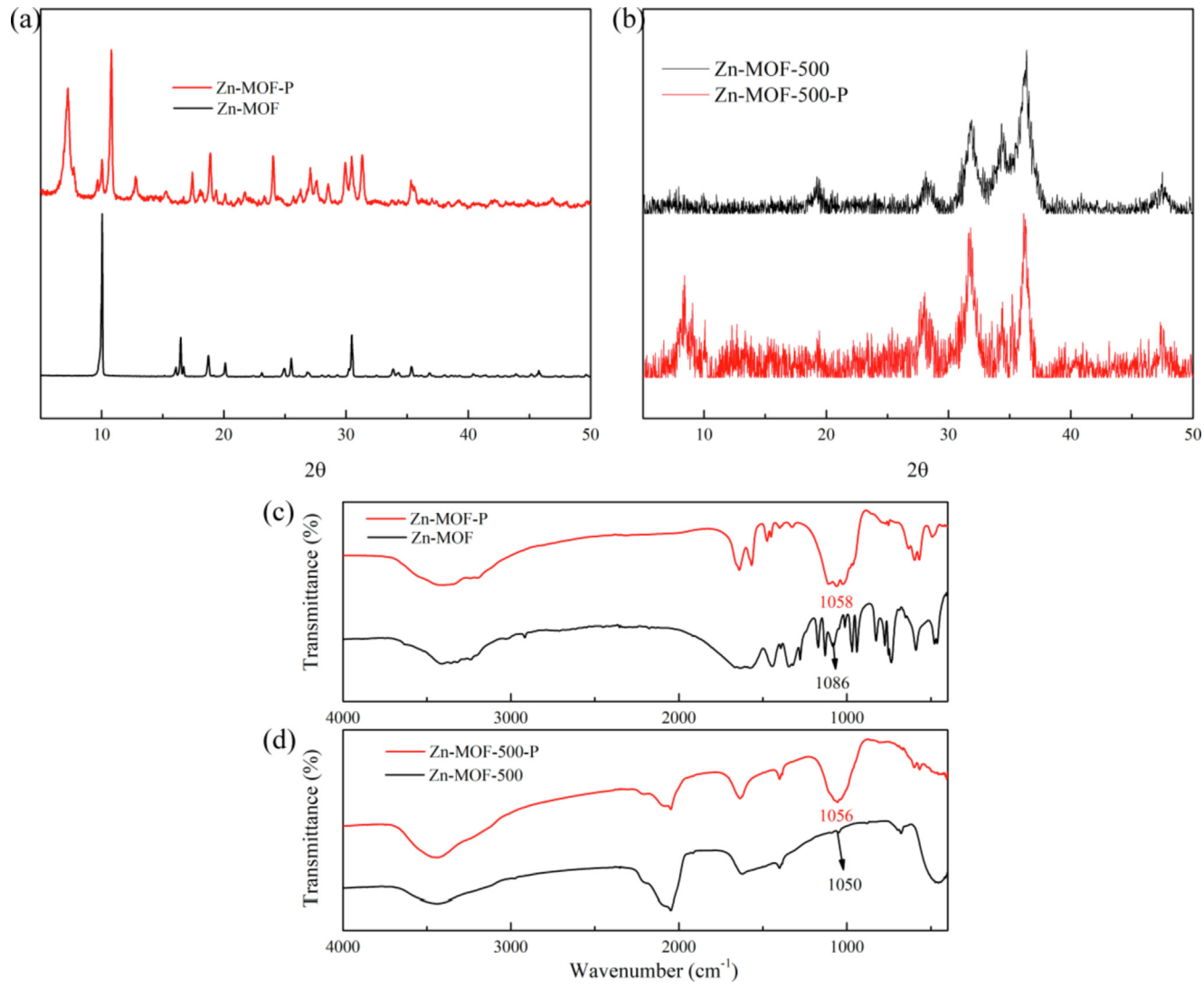

Fig. 7 (a, b) XRD peaks of Zn-MOF and Zn-MOF-500 before and after adsorption; (c, d) FT-IR spectra of Zn-MOF and Zn-MOF-500 before and after adsorption.

3.10. Xps

To obtain further information on the mechanism of phosphate adsorption, the XPS spectra of **Zn-MOF**, **Zn-MOF-500**, **Zn-MOF-P**, and **Zn-MOF-500-P** were obtained (He et al., 2020b; Liu et al., 2021) (Fig. 8). The peak positions of the main elements were found to remain unchanged before and after carbonization (Fig. 8b). When compared with the XPS survey spectra of **Zn-MOF** and **Zn-MOF-500**, it was found that a new peak corresponding to the P 2p XP spectral region appeared in the XPS survey spectra of **Zn-MOF-P** and **Zn-MOF-500-P**, indicating that the material adsorbs and fixes phosphate very well (Fig. 8a and b). By comparing the XPS N1s and O1s of **Zn-MOF** (Fig. 8c and d), the binding energy of N1s in **Zn-MOF-500** and the binding energy of O1s in **Zn-MOF-500** appear a new peak. This is because the structure of **Zn-MOF** was partially destroyed and some zinc oxide was produced during carbonization.

By comparing Fig. 8c **Zn-MOF O1s with** Fig. 8c **Zn-MOF-P O1s**, the lattice water peak (533.00 eV) (Huang et al., 2021) disappeared after adsorption of phosphate, the peak at 523.60 eV in Zn-MOF-P O1s was assigned to the hydroxyl group (P-OH) in HPO_4^{2-} (Huang et al., 2021), and the peak at 531.40 eV was assigned to Zn-O-P/P = O group (Huang et al., 2021), which indicated that Zn of Zn-MOF forms a strong Zn-O-P bond with phosphate.

In Fig. 8c Zn-MOF-500 O1s, the ZnO peak appeared at 530.20 eV, which indicated that a part of zinc oxide was produced after carbonization. Comparing Zn-MOF-500-P O1s with Zn-MOF-500, the amount of Zn-O peak (531.60 eV) (Zhang et al., 2021a, 2021b, 2021c) was greatly reduced, and Zn—O—P, P═O groups peak (531.40 eV) (Huang et al., 2021) appeared, which indicated the Zn on the undamaged part of the Zn-MOF produced Zn—O—P strong bonds with the phosphate. Moreover, the ZnO peak disappeared in Fig. 8c Zn-MOF-500-P which indicated that all ZnO of Zn-MOF-500 participated in the adsorption. In Fig. 8d, the peaks did not have any change after adsorption, indicating that N did not participate in the phosphate adsorption.

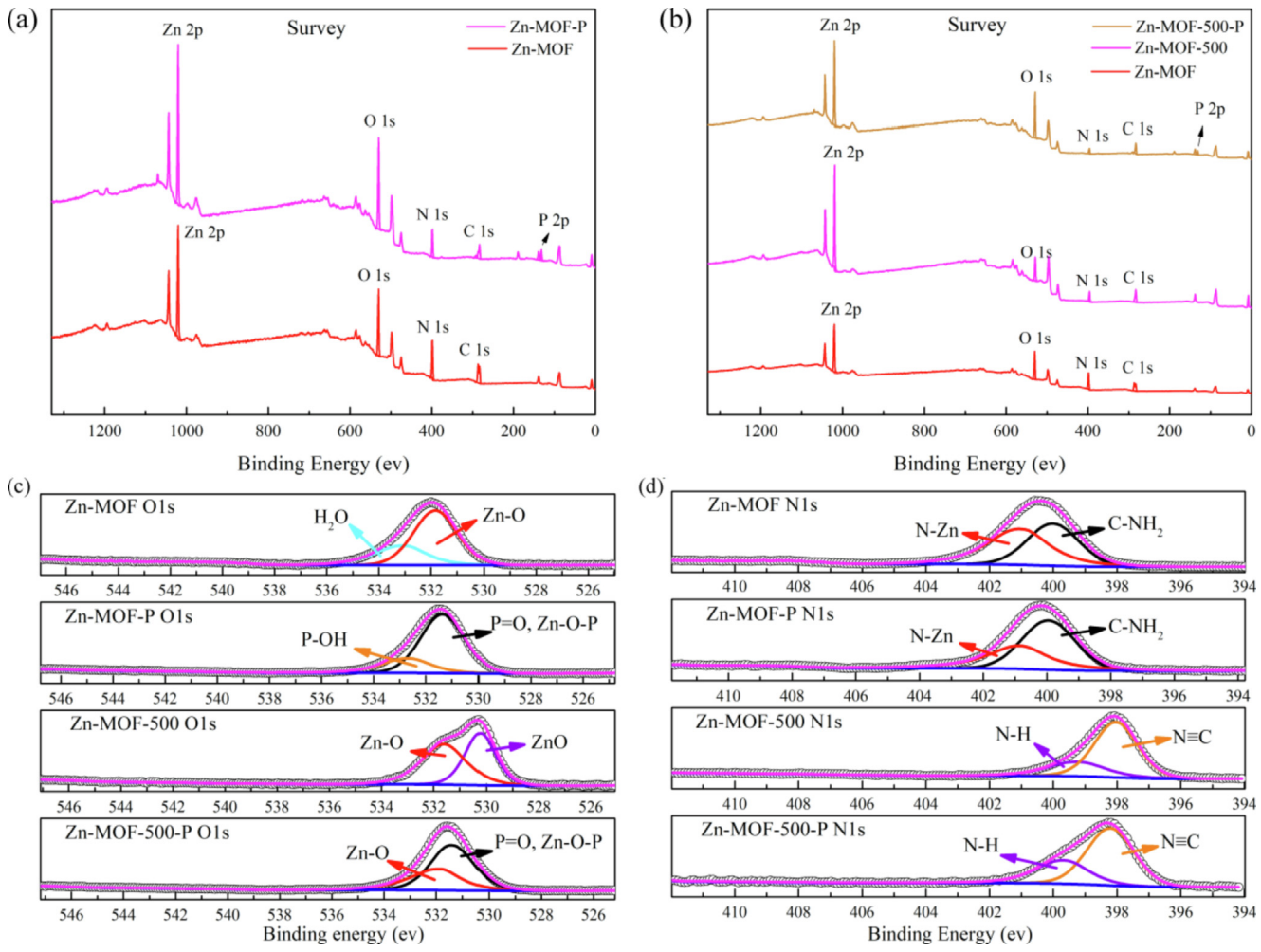

Fig. 8 (a, b) XPS survey spectrum of **Zn-MOF, Zn-MOF-P, Zn-MOF-500** and **Zn-MOF-500-P**; (c) Comparison of XPS O1s of **Zn-MOF, Zn-MOF-P, Zn-MOF-500** and **Zn-MOF-500-P**; (d) Comparison of XPS N1s of **Zn-MOF, Zn-MOF-P, Zn-MOF-500** and **Zn-MOF-500-P.**

In conclusion, according to the results of XPS O1s analysis (Fig. 8c), a large number of Zn—O—P peaks appeared in Zn-MOF and Zn-MOF-500 after adsorption, which mainly indicates Zn—O—P links played a major role in adsorption (Wang et al., 2020). Moreover, another key interaction was the electrostatic attraction between phosphate anions and Zn-MOF-500 (Fig. 3a).

By analyzing the P2p XPS spectral regions of the phosphate ion of **Zn-MOF-P** and **Zn-MOF-500-P** (Fig. S8), it was found that the P2p3/2 position in **Zn-MOF-P** and **Zn-MOF-500-P** was at 133.14 and 133.34 eV, respectively, which indicated that phosphate was mainly present in the form of zinc hydrogen phosphate or zinc phosphate in the material.

3.11. SEM and EDS (Energy dispersive Spectrometer)

A comparison of the morphologies of **Zn-MOF** and **Zn-MOF-500** in Fig. 9a and b, respectively, showed that there was a change in the surface morphology of the material. It was observed that several obvious pores and gullies appear, the pores were connective (Fig. S9), and the surface roughness was enhanced after carbonization. From the morphology of **Zn-MOF-P** (Fig. 9c) and the analysis of its EDS spectrum (Fig. S10c), phosphate was found to be adsorbed on the surface of **Zn-MOF** and the surface roughness of the material was changed to a certain extent. At the same magnification (3000 times), we found that the morphology of the material changed from regular block crystals of **Zn-MOF** to cluster-shaped crystal structure of **Zn-MOF-P** (Fig. 9a and 9c). For clearer observation the **Zn-MOF-P**, the magnification is adjusted to 7000 times (Fig. 9e). From Fig. 9e, it can be found that the cluster-shaped crystals of **Zn-MOF-P** observed at 3000 times (Fig. 9c) are actually formed by the stacking of many small strip crystals at 7000 times (Fig. 9e). The results show that the stability of **Zn-MOF** in the adsorption process is not good, but it still has high crystallinity, which is consistent with the experimental results of XRD above (Fig. 7a). The mass fraction of phosphate in **Zn-MOF-P** was 9.40% (Table S5), which was lower than the phosphate content when the adsorbent was saturated (q_{max} = 123.44 mg/g, which is 12.344%), indicating that a part of the phosphate was adsorbed in the pores of the **Zn-MOF**.

The surface roughness of the **Zn-MOF-500** is improved after adsorbed the phosphate by comparing Fig. 9b and d,

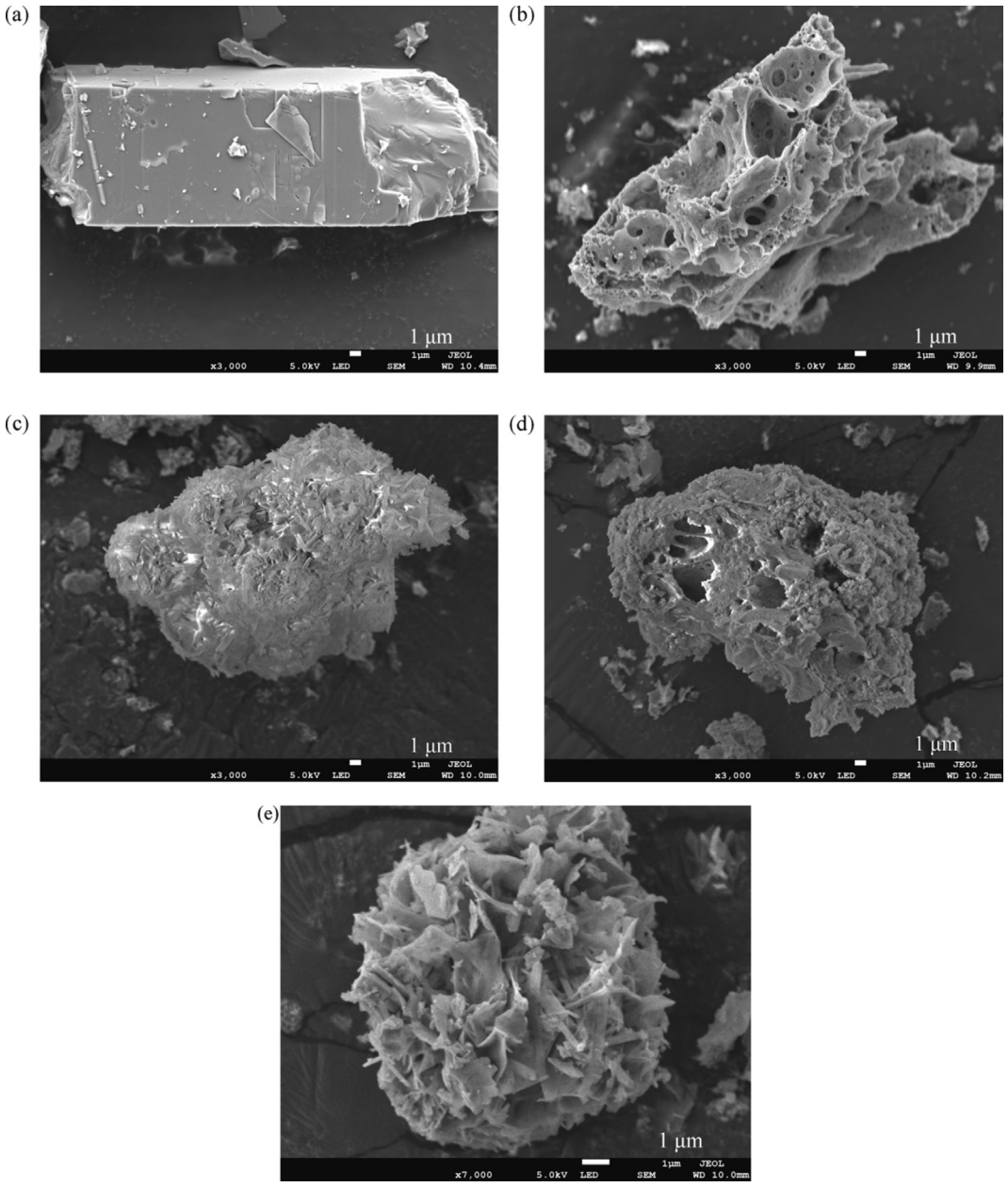

Fig. 9 SEM images of (a) **Zn-MOF**, (b) **Zn-MOF-500**, (c) **Zn-MOF-P** and (d) **Zn-MOF-500-P** in 3000 times; (e) Zn-MOF-**P** in 7000 times.

but the physical state of the **Zn-MOF-500 before and after adsorption** did not change to a large extent. According to Fig. 9d, the Phosphate was adsorbed on the surface of **Zn-MOF-500.** The mass fraction of phosphate in **Zn-MOF-500-P** was 1.08% (Table S5), which was much lower than the adsorption saturation of the adsorbent; when the phosphate content (q_{max} = 226.07 mg/g, 22.607%), it shows that most of the phosphate in the **Zn-MOF-500-P** was adsorbed in the pores.

Compared with **Zn-MOF,** the appearance of **Zn-MOF-500** has changed greatly and many pores have appeared on the surface of **Zn-MOF-500** (Fig. 9a, and b). The result was consistent with the findings of the previous BET characterization, which states that the specific surface area was expanded by 16.73 times. As a result, most of the phosphate was adsorbed in the pores of **Zn-MOF-500-P**.

4. Conclusion

In this study, a novel zinc-based MOF (**Zn-MOF**) was synthesized using low-cost, low-toxic zinc acetate dihydrate metal salt as the metal source, and inexpensive H_2pda and 5-amino-1*H*-tetrazolium as the organic ligands; mass production of **Zn-MOF** was achieved. To further expand the adsorption capacity, **Zn-MOF-500** was prepared by carbonization. The two materials were mainly chemical adsorption through kinetic fitting; the maximum adsorption capacity of **Zn-MOF-500** was found to be 226.07 mg/g through isothermal fitting. However,

this value of **Zn-MOF-500** was second only to that of **CM-300 (R)**. Because **CM-300(R)** was prepared using poisonous hydrazine hydrate, **Zn-MOF-500** was more suitable for practical purposes.

Acknowledgements

This work was supported by the Nature Science Foundation of China (No. 21861014), the Program of the Collaborative Innovation Center for Exploration of Hidden Nonferrous Metal Deposits and Development of New Materials in Guangxi (No. GXYSXTZX2017-II-3), the Talent introduction program of Guangdong Institute of Petrochemical Technology (No. 2020rc033).

Appendix A. Supplementary material

Deposition Number 2153990 was the CCDC numbers for **Zn-MOF**. The data for **Zn-MOF** is available for free at http://www.ccdc.cam.ac.uk, or by contacting The Cambridge Crystallographic Data Centre, 12 Union Road, Cambridge CB2 1EZ, UK; fax: +44 1223 336033. Electronic supplementary information (ESI) available: Materials and chemicals, Scheme and characterization of adsorption experiment, crystallographic details, selected bond lengths and angles, SHAPE data of **Zn-MOF**, FTIR curves, **Zn-MOF** stacking diagram, XRD spactra of **Zn-MOF**, Distribution of various forms of phosphate in water at different temperatures, Adsorption kinetics of phosphate onto (a) **Zn-MOF** and (b) **Zn-MOF-500**, Recyclability test of **Zn-MOF** and **Zn-MOF-500** in water at 25 ^{o}C, Nitrogen adsorption-desorption isotherm and pore size distribution of **Zn-MOF** (a,b) and **Zn-MOF-500**(c,d), TGA of **Zn-MOF** and **Zn-MOF-500**, Comparison of XPS P2p of the (a) **Zn-MOF-P** and (b) **Zn-MOF-500-P.** SEM images of **Zn-MOF-500** before the adsorption of phosphate under 20000 times, The EDS energy spectrum, EDS Energy Spectrum Data Sheet. Supplementary data to this article can be found online at https://doi.org/10.1016/j.arabjc.2022.103955.

References

Acharya, L., Nayak, S., Pattnaik, S.P., Acharya, R., Parida, K., 2020. Resurrection of boron nitride in p-n type-II boron nitride/B-doped-g-C3N4 nanocomposite during solid-state Z-scheme charge transfer path for the degradation of tetracycline hydrochloride. J. Colloid Interf. Sci. 566, 211–223. https://doi.org/10.1016/j.jcis.2020.01.074.

Bacelo, H., Pintor, A.M.A., Santos, S.C.R., Boaventura, R.A.R., Botelho, C.M.S., 2020. Performance and prospects of different adsorbents for phosphate uptake and recovery from water. Chem. Eng. J. 381, 12256. https://doi.org/10.1016/j.cej.2019.122566.

Chen, G.-H., Li, H.-Z., He, Y.-P., Zhang, S.-H., Yi, X., Ling, F.-P., Zhang, L., Zhang, J., 2020. Ti_4(embonate)$_6$ Based Cage-Cluster Construction in a Stable Metal−Organic Framework for Gas Sorption and Separation. Cryst. Growth. Des. 20, 29–32. https://doi.org/10.1021/acs.cgd.9b01297.

Chen, Z., Li, P., Zhang, X., Li, P., Wasson, M.C., Islamoglu, T., Stoddart, J.F., Farha, O.K., 2019. Reticular access to highly porous acs -MOFs with rigid trigonal prismatic linkers for water sorption. J. Am. Chem. Soc. 141, 2900–2905. https://doi.org/10.1021/jacs.8b13710.

Dolomanov, O.V., Bourhis, L.J., Gildea, R.J., Howard, J.A.K., Puschmann, H., 2009. OLEX2: A complete structure solution, refinement and analysis program. J. Appl. Cryst. 42, 339–341. https://doi.org/10.1107/s0021889808042726.

Eltaweil, A.S., Elshishini, H.M., Ghatass, Z.F., Elsubruiti, G.M., 2020. Ultra-high adsorption capacity and selective removal of Congo red over aminated graphene oxide modified Mn-doped UiO-66 MOF. Powder Technol. 379, 407–416. https://doi.org/10.1016/j.powtec.2020.10.084.

Gao, L., Li, Z., Yi, W., Li, Y., Zhang, P., Zhang, A., 2021. Impacts of pyrolysis temperature on lead adsorption by cotton stalk-derived biochar and related mechanisms. J. Environ. Chem. Eng. 9,. https://doi.org/10.1016/j.jece.2021.105602 105602.

Guan, H.-Y., LeBlanc, R.J., Xie, S.-Y., Yue, Y., 2018. Recent progress in the syntheses of mesoporous metal–organic framework materials. Coordin. Chem. Rev. 369, 76–90. https://doi.org/10.1016/j.ccr.2018.05.001.

Guan, T., Li, X., Fang, W., Wu, D., 2020. Efficient removal of phosphate from acidified urine using UiO-66 metal organic frameworks with varying functional group. App. Surf. Sci. 501,. https://doi.org/10.1016/j.apsusc.2019.144074 144074.

Ghosh, A., Das, G., 2021. Facile synthesis of Sn(II)-MOF using waste PET bottles as an organic precursor and its derivative SnO_2 NPs: Role of surface charge reversal in adsorption of toxic ions. J. Environ. Chem. Eng. 9,. https://doi.org/10.1016/j.jece.2021.105228 105288.

He, J., Xu, Y., Shao, P., Yang, L., Sun, Y., Yang, Y., Cui, F., Wang, W., 2020a. Modulation of coordinative unsaturation degree and valence state for cerium-based adsorbent to boost phosphate adsorption. Chem. Eng. J. 394,. https://doi.org/10.1016/j.cej.2020.124912 124912.

He, J., Xu, Y., Wang, W., Hu, B., Wang, Z., Yang, X., Wang, Y., Yang, L., 2020b. Ce(III) nanocomposites by partial thermal decomposition of Ce-MOF for effective phosphate adsorption in a wide H range. Chem. Eng. J. 379,. https://doi.org/10.1016/j.cej.2019.122431 122431.

Huang, C., Zhang, H., Zheng, K., Zhang, Z., Jiang, Q., Li, J., 2021. Two-dimensional hydrophilic ZIF-L as a highly-selective adsorbent for rapid phosphate removal from wastewater. Sci. Total Environ. 785,. https://doi.org/10.1016/j.scitotenv.2021.147382 147382.

Karimi, H., Heidari, M.A., Emrooz, H.B.M., Shokohimehr, M., 2020. Carbonization temperature effects on adsorption performance of metal-organic framework derived nanoporous carbon for removal of methylene blue from wastewater; experimental and spectrometry study. Diam. Relat. Mater. 108,. https://doi.org/10.1016/j.diamond.2020.107999 107999.

Lian, Q., Islam, F., Ahmad, Z.U., Lei, X., Depan, D., Zappi, M., Gang, D.D., Holmes, W., Yan, H., 2021. Enhanced adsorption of resorcinol onto phosphate functionalized graphene oxide synthesized via Arbuzov Reaction: A proposed mechanism of hydrogen bonding and π-π interactions. Chemosphere 280,. https://doi.org/10.1016/j.chemosphere.2021.130730 130730.

Li, S., Zhang, Q., Yin, C., Chen, J., Yang, X., Wang, S., 2021. Tuning microscopic structure of Al-based metal-organic frameworks by changing organic linkers for efficient phosphate removal. J. Clean. Prod. 292,. https://doi.org/10.1016/j.jclepro.2021.125998 125998.

Lin, K.-Y.-A., Chen, S.-Y., Jochems, A.P., 2015. Zirconium-based metal organic frameworks: Highly selective adsorbents for removal of phosphate from water and urine. Mater. Chem. Phys. 160, 168–176. https://doi.org/10.1016/j.matchemphys.2015.04.021.

Liu, W.-B., Cui, G.-N., Wang, H., Zhang, D., Wu, R., Li, L., Zhang, X., Fan, Y.-H., 2020. Efficient and selective adsorption of dye in aqueous environment employing a functional Zn(II)-based metal

organic framework. J. Solid State Chem. 292,. https://doi.org/10.1016/j.jssc.2020.121740 121740.

Liu, X., Pang, H., Liu, X., Li, Q., Zhang, N., Mao, L., Qiu, M., Hu, B., Yang, H., Wang, X., 2021. Orderly Porous Covalent Organic Frameworks-based Materials: Superior Adsorbents for Pollutants Removal from Aqueous Solutions. The innovation 2,. https://doi.org/10.1016/j.xinn.2021.100076 100076.

Nuryadin, A., Imai, T., Kanno, A., Yamamoto, K., Sekine, M., Higuchi, T., 2021. Phosphate adsorption and desorption on two-stage synthesized amorphous-ZrO_2/Mg–Fe layered double hydroxide composite. Mater. Chem. Phys. 266,. https://doi.org/10.1016/j.matchemphys.2021.124559 124559.

Pandi, K., Choi, J., 2021. Selective removal of anionic ions from aqueous environment using iron-based metal-organic frameworks and their mechanistic investigations. J. Mol. Liq. 329,. https://doi.org/10.1016/j.molliq.2021.115367 115367.

Rukayat, O., Usman, M.F., Elizabeth, O.M., Abosede, O.O., Faith, I. U., 2021. Kinetic Adsorption of Heavy Metal (Copper) On Rubber (Hevea Brasiliensis) Leaf Powder. South African J. Chem. Eng. 37, 74–80. https://doi.org/10.1016/j.sajce.2021.04.004.

Sheldrick, G.M., 2008. A short history of SHELX. Acta. Crystallogr. A. 64, 112–122. https://doi.org/10.1107/s0108767307043930.

Sheldrick, G.M., 2015. Crystal structure refinement with SHELXL. Acta. Crystallogr. C. Struct. Chem. 71, 3–8. https://doi.org/10.1107/s2053229614024218.

Solanki, V.A., Borah, B., 2019. Ranking of Metal-Organic Frameworks (MOFs) for separation of Hexane Isomers by Selective Adsorption. Ind. Eng. Chem. Res. 58, 20047–20065. https://doi.org/10.1021/acs.iecr.9b03533.

Sumida, K., Rogow, D.L., Mason, J.A., McDonald, T.M., Bloch, E. D., Herm, Z.R., Bae, T.-H., Long, J.R., 2012. Carbon dioxide capture in metal-organic frameworks. Chem. Rev. 112, 724–781. https://doi.org/10.1021/cr2003272.

Tang, X., Luo, Y., Zhang, Z., Ding, W., Liu, D., Wang, J., Guo, L., Wen, M., 2021. Effects of functional groups of $–NH_2$ and $–NO_2$ on water adsorption ability of Zr-based MOFs (UiO-66). Chem. Phys. 543,. https://doi.org/10.1016/j.chemphys.2021.111093 111093.

Wang, S.-T., Zheng, X., Zhang, S.-H., Li, G., Xiao, Y., 2021. Study of GUPT-2, a Water-Stable Zinc-based Metal-Organic Framework as a Highly Selective and Sensitive Fluorescence Sensor in the Detection of Al^{3+} and Fe^{3+} Ions. CrystEngComm. 23, 4059–4068. https://doi.org/10.1039/d1ce00323b.

Wang, Y., Zhao, W., Qi, Z., Zhang, L., Zhang, Y., Huang, H., Peng, Y., 2020. Designing ZIF-8/hydroxylated MWCNT nanocomposites for phosphate adsorption from water: Capability and mechanism. Chem. Eng. J. 394,. https://doi.org/10.1016/j.cej.2020.124992 124992.

Wu, D., Zhang, P.-F., Yang, G.-P., Hou, L., Zhang, W.-Y., Han, Y.-F., Liu, P., Wang, Y.-Y., 2021a. Supramolecular control of MOF pore properties for the tailored guest adsorption/separation applications. Coordin. Chem. Rev. 434. https://doi.org/10.1016/j.ccr.2020.213709.

Wu, D., Cheng, J., Wang, M., Liu, J., Jin, J., Yang, G., Zhang, W., Wang, Y.-Y., 2021b. Design and preparation of new luminescent metal–organic frameworks and different doped isomers: sensing pollution ions and enhancement of gas capture capacity. Inorg. Chem. Front 8, 286. https://doi.org/10.1039/D0QI01088J.

Xie, Q., Li, Y., Lv, Z., Zhou, H., Yang, X., Chen, J., Guo, H., 2017. Effective Adsorption and removal of phosphate from aqueous solutions and eutrophic water by Fe-based MOFs of MIL-101. Sci. Rep.-UK 7, 3316. https://doi.org/10.1038/s41598-017-03526-x.

Zhang, M.-Y., Wang, X.-P., Lin, R., Liu, Y., Chen, F.-S., Cui, L.-S., Meng, X.-M., Hou, J., 2021a. Improving the hydrostability of ZIF-8 membrane by biomolecule towards enhanced nanofiltration performance for dye removal. J. Membrane Sci. 618,. https://doi.org/10.1016/j.memsci.2020.118630 118630.

Zhang, S., Chen, Z., Zhou, T., Li, G., 2022. Zn Metal-Organic Framework with High Stability and Sorption Selectivity for CO_2. Organometallics. 41, 829–835. https://doi.org/10.1021/ACS.ORGANOMET.2C00054.

Zhang, X., Sun, F., He, J., Xu, H., Cui, F., Wang, W., 2017. Robust phosphate capture over inorganic adsorbents derived from lanthanum metal organic frameworks. Chem. Eng. J. 326, 1086–1094. https://doi.org/10.1016/j.cej.2017.06.052.

Zhang, X., Xiong, B., Li, J., Qian, L., Liu, L., Liu, Z., Fang, P., He, C., 2019. Dependence of Dye Molecules Adsorption Behaviors on Pore Characteristics of Mesostructured MOFs Fabricated by Surfactant Template. ACS Appl. Mater. Inter. 11, 31441–31451. https://doi.org/10.1021/acsami.9b06517.

Zhang, Y., Chen, Z., Liu, X., Dong, Z., Zhang, P., Wang, J., Deng, Q., Zeng, Z., Zhang, S., Deng, S., 2020. Efficient SO_2 removal using a microporous metal−organic framework with molecular sieving effect. Ind. Eng. Chem. Res. 59, 874–882. https://doi.org/10.1021/acs.iecr.9b06040.

Zhang, Z., Chen, Z., Xiao, Y., Yi, M., Zheng, X., Xie, M., Shen, M., 2021a. Study of the dynamic adsorption and the effect of the presence of different cations and anions on the adsorption of As(V) on GUT-3. Appl. Organomet. Chem. 35,. https://doi.org/10.1002/aoc.6289 e6289.

Zhang, Z., Zhou, C., Wu, H., Liu, J., Yang, H., 2021b. Molecular study of heterogeneous mercury conversion mechanism over Cu-MOFs: Oxidation pathway and effect of halogen. Fuel 290,. https://doi.org/10.1016/j.fuel.2020.120030 120030.

Zhang, Z., Chen, Y., Wang, Z., Hu, C., Ma, D., Chen, W., Ao, T., 2021c. Effective and structure-controlled adsorption of tetracycline hydrochloride from aqueous solution by using Fe-based metal-organic frameworks. Appl. Surf. Sci. 542,. https://doi.org/10.1016/j.apsusc.2020.148662 148662.